Journal of Alloys and Compounds 509 (2011) 1901–1905

Contents lists available at ScienceDirect

Journal of Alloys and Compounds

journal homepage: www.elsevier.com/locate/jallcom

Structural, electronic and optical properties of $BiFeO_3$ studied by first-principles

Kun Liu, Huiqing Fan*, Pengrong Ren, Chao Yang

State Key Laboratory of Solidification Processing, School of Materials Science and Engineering, Northwestern Polytechnical University, Xi'an 710072, China

ARTICLE INFO

Article history:
Received 5 July 2010
Received in revised form 10 October 2010
Accepted 21 October 2010
Available online 29 October 2010

Keywords:
$BiFeO_3$
First-principle
Electronic property
Optical property

ABSTRACT

The structural, electronic and optical properties of $BiFeO_3$ (BFO) were investigated employing the first-principles within generalized gradient approximation (GGA). The magnetic moments were balanced out each other by the two irons spinning oppositely in a cell. The band gap of BFO was found to be 2.5 eV by the electronic structure calculation. Analysis of the density of states indicated that the valence band was consisted with Fe-d and O-p states, and the conduction band was composed of Fe-d and Bi-p states. The dielectric function, absorption, refractive index, extinction coefficient, reflectivity and electron energy loss were calculated for radiation up to 31 eV in order to understand optical properties of BFO. The reasons of the absorption were discussed.

1. Introduction

Multiferroic materials [1–5] have coupled electric, magnetic, and/or structural order parameters that result in simultaneous ferromagnetic, ferroelectric, and/or ferroelastic behavior. Significantly, multiferroics may lead to a new generation of memory devices [6,7] that can be electrically written and magnetically read [5,7]. Room-temperature multiferroic $BiFeO_3$ (BFO) is a rhombohedrally distorted ferroelectric perovskite with space group R3c below the Curie temperature ($T_C \approx 1100$ K), and shows antiferromagnetism blow Néel temperature ($T_N \approx 643$ K) [8,9]. These unique multiferroic properties make BFO attracting great interest for potential applications in novel magnetoelectric devices and fuel considerable theoretical and experimental research [10–13].

Much research has been reported in the open literature aimed at improving the electrical and magnetic properties of BFO doped with various metal oxides by the theoretical and experimental methods [14–24]. Du et al. [14] found that the dielectric constant of $Bi_{1-x}La_xFeO_3$ sample increased after La doping. Uniyal and Yadav [15] synthesized the nanocomposites of $ZnFe_2O_4$–$BiFeO_3$ by sol–gel technique and found that the magnetic behavior was strongly dependent on the annealing temperature. Simões et al. [16] deposited the Nb doped $BiFeO_3$ films by soft chemical method and found that the Nb dopant was effective in improving electrical properties of $BiFeO_3$ films. Liu et al. [17] prepared the Ce-doped $Bi_{1-x}Ce_xFeO_3$ thin films on $Pt/TiO_2/SiO_2/Si$ substrates by chemical solution deposition and found that the saturation magnetization increased with the increase of Ce content. Kazhugasalamoorthy et al. [18] investigated the properties of pure and rare earth modified $BiFeO_3$ ceramics. Zhang et al. [19] found that the leakage current decreased with the increasing Eu concentration. Another research group investigated the band gap, stress constant and optical properties, respectively [20]. It was reported that the direct 300 K charge gap was observed at 2.67 eV. Mishra and Qi [21] calculated the band gap of the Ni-doped $BiFeO_3$ (2.75 eV) prepared by using sol–gel method from the absorption data. Theoretically, Baettig et al. [22] calculated the magnetic nearest-neighbor coupling constants for $BiFeO_3$, Bi_2FeCrO_6 and $BiCrO_3$ by employing the LDA + U method. Their results provided a possibility for designing a multiferroic material with large magnetization above room temperature. In addition, Zhu et al. [23] studied the properties of $BiFeO_3$ (1 1 1) surface by using the full-potential augmented plane wave method within the LSDA + U. Wang et al. [24] obtained the elastic compliance coefficients of $BiFeO_3$ by using density functional theory. Simulating the antiferromagnetic property of $BiFeO_3$ was ignored in their work.

In the present work, the spin directions of Fe atoms in a cell were set to be aligned in opposite senses along the [1 1 1] direction to simulate the antiferromagnetic property. This assumption is justified because BFO is in fact nearly antiferromagnetic, since it rather exhibits a spiral spin structure, which requires building much larger supercells containing thousands of atoms and considering additional interactions. Our assumption should qualitatively apply to BFO. The band structure, electronic, optical and Mulliken charges properties of BFO were calculated by using a series of first-principles. The optical properties, which contain the frequency-dependent absorption spectra, reflectivity, refractive index, dielectric function and loss function, were investigated.

* Corresponding author. Tel.: +86 29 88494463; fax: +86 29 88492642.
E-mail address: hqfan3@163.com (H. Fan).

0925-8388/$ – see front matter © 2010 Elsevier B.V. All rights reserved.
doi:10.1016/j.jallcom.2010.10.084

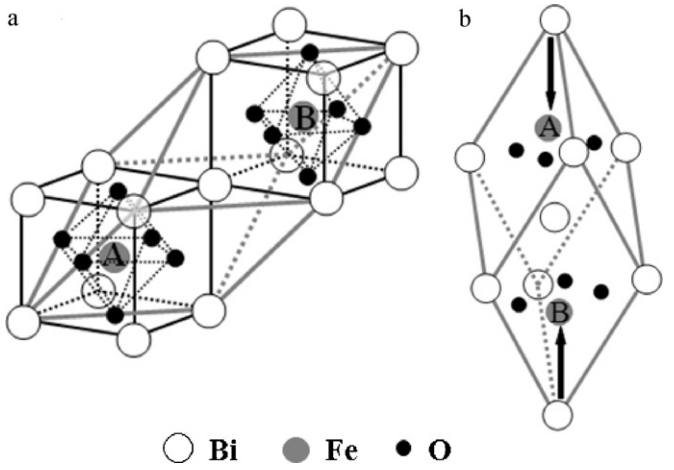

Fig. 1. The pseudocubic cell (a) and rhombohedral cell (b) of the structure of the R3c phase of $BiFeO_3$. The Fe atom at A site and at B site is intercalated spinning downward and spinning upward, respectively.

The crystal field theory was employed to explain the results of the absorption spectra.

2. Computational methods

The first-principles calculation is performed using density function theory (DFT) [25] within the generalized gradient approximation (GGA) with the correction of Perdew–Burke–Ernzerhof for the exchange-correction potential [26,27] as implemented in CASTEP code. In order to build the model of BFO, the Materials Visualizer is implemented. The BFO model is shown in Fig. 1. It is seen that the perfect BFO cell consists of two Bi, two Fe and six O centered at Bi^{3+}. The electronic configuration of Fe atom, which is ferric iron in BFO, is $3d^6 4s^2$. According to the Hund's rules, the system is more stable when the orbital is full, half-full or empty. Thus, Fe atom contributes three electrons, two electrons of that in 4s orbit and one of that in 3d orbit, to help the unpaired electron of O pairing. At the same time, other five unpaired electrons in 3d orbit will hold the same spin directions but different magnetic quantum numbers. On the basis of valence bond theory, it is easy to form outer-orbital coordination compound for the large electronegativity of O when oxygen atom coordinates the central atom. To constitute the FeO_6 octahedral, the oxygen anions furnish the lone-pair electron to occupy the empty bands which are supplied by the 4s4p4d hybridized orbits of Fe atom in the central of the octahedral. Thus, the Fe atom, which has five unpaired electron in 3d orbit, belongs to high spin states. In a word, it is reasonable for us to set two Fe^{3+} ions in a cell both at high spin states but opposite directions to simulate the antiferromagnetic property of BFO. For the R3c antiferromagnetic state, there is one possibility of lower symmetry (↑↓) [28], where the arrows represent the relative orientation of spins on positions A and B in Fig. 1. The total charge of the cell are set zero.

In this paper, CASTEP code has been used for the ground-state electronic structure calculations under DFT method theoretically based on GGA. The different cut-off energy is employed to calculate process geometry optimization, and the correlation between total energy and cut-off energy is shown in Fig. 2. Neighboring difference between 340 and 380 eV is smaller than 1×10^{-4} eV, so the plane-wave cut-off energy of 340 eV is chosen. Ultrasoft pseudopotentials [29] are used for the Bi, Fe and O atoms. The smaller the energy, stress and displacement of system are, the more stable the system is, so optimal atomic positions are determined until the following conditions are satisfied: (i) the maximal change of energy per atom is smaller than 1×10^{-5} eV; (ii) the maximal displacement is smaller than 1×10^{-4} Å; (iii) the maximal force on them is smaller than 1×10^{-2} eV/Å; (iv) SCF tolerance = 1×10^{-6} eV/atom. All other calculations are performed on the basis of the optimized lattice structure. Then the band structure, density of states, population analysis and optical properties are calculated.

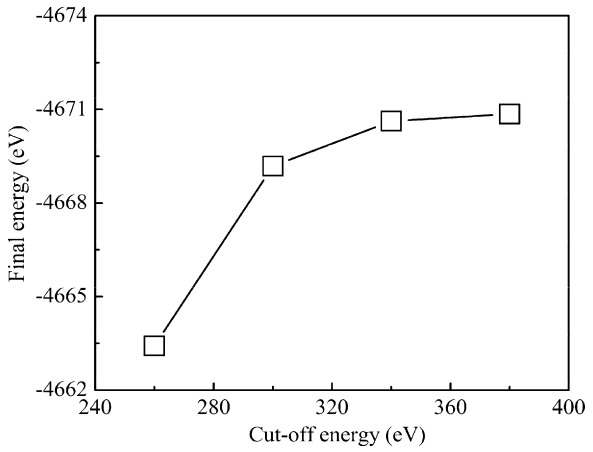

Fig. 2. The variation in system energy as a function of cut-off energy of $BiFeO_3$.

3. Results and discussion

3.1. Structural properties

The lattice parameters acquired from full structural optimization of BFO are listed in Table 1. It is seen that the results are in better agreement with experimental mean values, which have only a 0.56% underestimation of the equilibrium volume compared with the experimental average value. But the length and angle of the lattice vector are a little longer and smaller than the experimental mean values, respectively. It is indicated that there is a more serious inner structural distortion in geometry optimization in our simulation than the experimental [11,30–32]. This is attributed to no defect in ideal crystal, which is different from the practical crystal. We find that the use of GGA + U makes the equilibrium volume have a 2.4% overestimation than the experimental value. Accord-

Table 1
Experimental and calculated lattice constant a (Å), rhombohedral angel α (°), volume V (Å^3) and atomic fractional coordinates for $BiFeO_3$ in R3c structure, where the rhombohedral structure was used.

	a	α	V	Fe (x, x, x)	O (x, y, z)
Exp.[a]	5.634	59.348	124.6	0.221	0.528 0.395 0.933
Exp.[b]	5.637	59.344	124.8	0.221	0.524 0.397 0.934
Exp.[c]	5.630	59.343	124.3	0.221	0.523 0.422 0.939
Exp.[d]	5.635	59.348	124.6	0.220	0.527 0.937 0.396
Cal.[e]	5.459	60.360	116.0	0.231	0.542 0.943 0.398
Cal.[f]	5.697	59.235	128.5	0.223	0.534 0.936 0.387
Cal.[g]	5.500	60.180	115.0	0.231	0.399 0.541 0.946
Cal.[h]	5.660	57.320	120.4	0.221	0.530 0.936 0.390
Cal.[i]	5.672	59.240	127.7	0.224	0.535 0.937 0.388
Cal.[j]	**5.669**	**58.349**	**124.0**	**0.222**	**0.368 0.551 0.929**

[a] Ref. [10].
[b] Ref. [30].
[c] Ref. [31].
[d] Ref. [32].
[e] Ref. [11], VASP-PAW-LDA.
[f] Ref. [5], VASP-PAW-GGA.
[g] Ref. [33], ABINIT-NCPP-LDA.
[h] Ref. [34], PWSCF-USPP-LDA.
[i] Ref. [35], WIEN2k–FP–LAPW–GGA.
[j] Present work, MS-CASTEP-USPP-GGA.

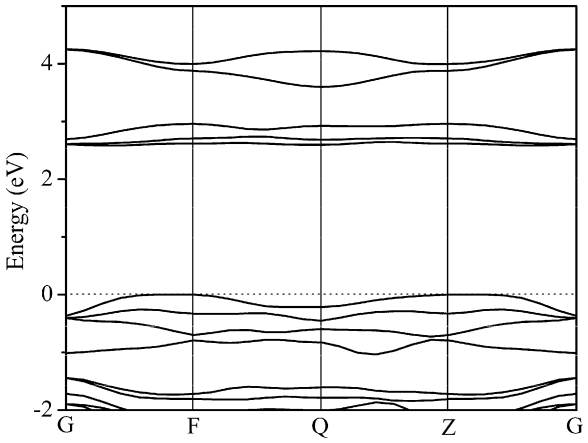

Fig. 3. Calculated energy band structure of $BiFeO_3$. The energy of the top of the valence band (E_F) is set to zero.

ing to the discussion above, the GGA is sufficient to describe the structure of BFO.

3.2. Electronic properties

The calculated energy band structure of BFO along the high symmetry directions in the Brillouin zone is shown in Fig. 3. The top of valence is set as zero energy level for BFO. To repair the systematic error of GGA, the scissors made a rigid upward shift of conductive bands by 1.4 eV to represent the experimental band gap [20].

The spin magnetic moment is provided by iron atoms of BFO. To simulate the antiferromagnetic order, two iron atoms are set spinning oppositely in a cell, then the magnetic moments are counteracted each other (A site spinning downward and B site spinning upward shown in Fig. 1). In ideal condition, there is no net magnetic moment in infinite periodic structures. As shown in Fig. 4, DOS of the atom spinning upward and downward are completely symmetry with no net magnetic moment.

To further elucidate the nature of the electronic band structure, the total and atomic site partial densities of states (PDOS) of BFO have been calculated shown in Fig. 5. The angular momentum character of the different structures can be identified from the PDOS. From the Fig. 5, the lower bands in the range of −11 to −9 eV are provided by Bi-6s states and the lone pair lying off center for this site is difficult to be infected by other atoms. Thus, the origin of ferroelectricity in BFO is better described as originating from dynamic O

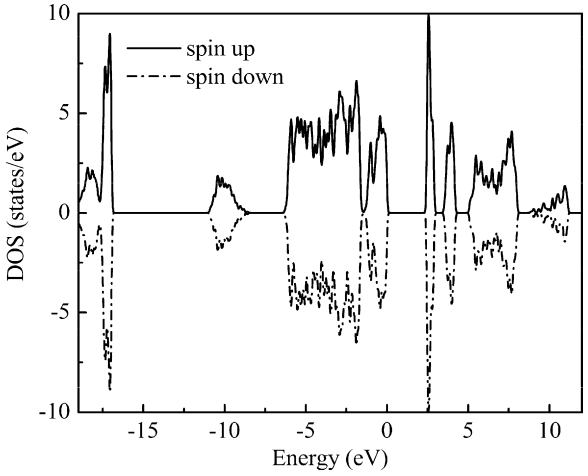

Fig. 4. The calculated total densities of states, showing spin up and down of $BiFeO_3$.

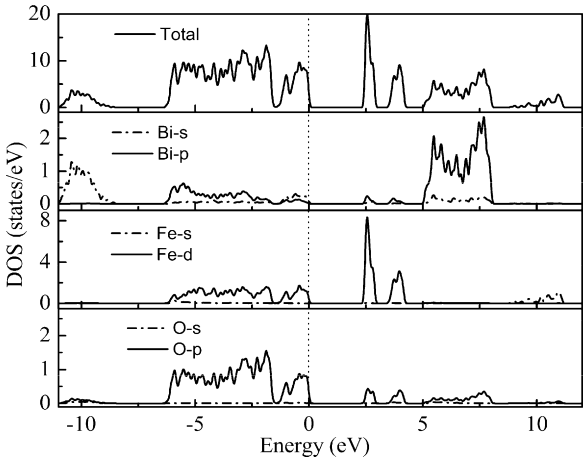

Fig. 5. The calculated total and partial densities of states in $BiFeO_3$ (only show spin up). From the top down, it is shown total density, the density of Bi, Fe, O atom in turn.

Table 2
Spilling parameters, atomic Mulliken charges and valence charges calculated for $BiFeO_3$.

Spilling parameter	Anion charge (e)	Cation charge (e)	Effective valence (|e|)
3×10^{-3}	O: −0.81	Fe: 0.83 Bi: 1.62	2.17 1.38

p–Bi p hybridization [36]. The top of the valence bands in the range of −6.5–0 eV is shown to be of predominantly O-p states character with minor contributions of Bi-p states and Fe-d states. At the lower conduction bands (2.5–4 eV), Fe-d states provide mostly and O-p states provide only a little. The middle conduction bands (6–8 eV) are occupied dominantly by Bi-p states, Fe-s states take over the range of 10–11 eV in the top of the conduction bands. From the Fig. 5, there are covalent bonding contributions between Fe and O atoms and between Bi and O atoms.

The Mulliken analysis is employed to calculate the spilling parameter, atomic charges (Table 2), populations and chemical bond lengths (Table 3). It is found that the spilling parameter for BFO system is very low which is reasonable to a good representation of the electronic bands using the initializing basis set. A spilling parameter in the region of 10^{-3} indicates that only approximately 0.3% of the valence charge has been missed in this work. The effective valences of the atoms are listed in Table 2. The effective valence is used as a measure of ionicity: a value of zero implies an ideal ionic bond and values greater than zero indicate increasing levels of covalence. It is indicated that there are more covalent bonding contributions between Fe and O atoms than between Bi and O atoms. Table 3 shows the populations for different species in the crystal. A value for the population close to zero indicates that there is no significant interaction between the electronic populations of the two atoms. It is also found that the bond length decreases with the increasing values of populations.

Table 3
Mulliken populations and bond length calculated from PW pseudopotential calculations for $BiFeO_3$.

Bond	Population (e)	Bond length (Å)
$O_{1,2,3}$–Fe_1	0.40	1.96
$O_{4,5,6}$–Fe_2	0.40	1.96
$O_{1,2,3}$–Bi_2	0.12	2.20
$O_{4,5,6}$–Bi_1	0.12	2.20

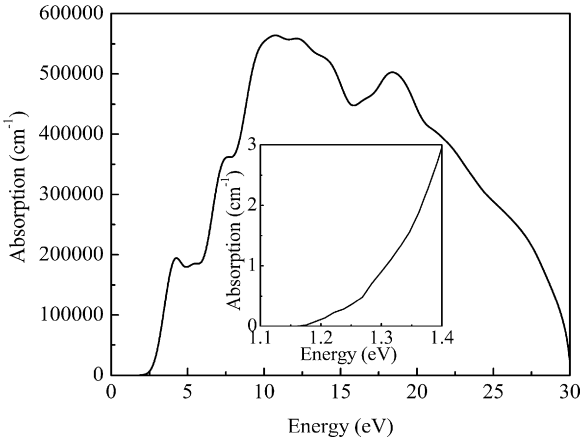

Fig. 6. Calculated absorption spectrum of $BiFeO_3$. The insert shows the dependence of the absorption on the energy with a range from 1.1 eV to 1.4 eV.

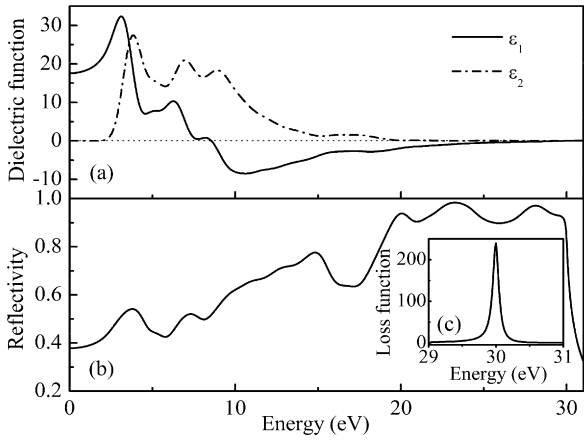

Fig. 7. Calculated the dielectric function $\varepsilon(\omega)$ (a), optical reflectivity spectrum $R(\omega)$ (b) and energy loss spectrum $L(\omega)$ (c) of $BiFeO_3$.

3.3. Optical properties

The complex dielectric constant in Eq. (1) describes the linear response of a system due to an external electromagnetic field with a small wave vector. In general, the difference between the propagation of an electromagnetic wave through vacuum and some other material can be described by a complex refractive index displayed in Eq. (2). The correlation between the dielectric function and refractive index can be shown in Eq. (3).

$$\varepsilon(\omega) = \varepsilon_1(\omega) + i\varepsilon_2(\omega), \tag{1}$$

$$N(\omega) = n(\omega) + ik(\omega), \tag{2}$$

$$\varepsilon(\omega) = N^2(\omega). \tag{3}$$

$$\varepsilon_2(\omega) = \left(\frac{\nu e^2}{2\pi\hbar m^2\omega^2}\right)\int d^3\boldsymbol{K}\sum_{nn'}\left|\left\langle \boldsymbol{K}n\left|\boldsymbol{P}\right|\boldsymbol{K}n'\right\rangle\right|^2 \times f(\boldsymbol{K}n)(1-f(\boldsymbol{K}n'))\delta(E_{\boldsymbol{K}n}-E_{\boldsymbol{K}n'}-\hbar\omega) \tag{4}$$

Here ω is the angular frequency. The imaginary part $\varepsilon_2(\omega)$ of the dielectric function can be thought of as detailing the real transition between occupied and unoccupied electric states and given by Eq. (4) [35]. Here $\hbar\omega$ is the energy of the incident photon, $\boldsymbol{P}$ is the momentum operator and $f(\boldsymbol{K}n)$ is the Fermi function. The other symbols have their usual meanings. The real part $\varepsilon_1(\omega)$ of the dielectric function can be obtained by the Kramers–kroning transform which links the real and imaginary parts. We have calculated the absorption, refractive index and other optical properties, which can be derived from the dielectric function.

The calculated absorption spectrum is shown in Fig. 6, and the inset shows the dependence of the absorption on the energy with a range of 1.1–1.4 eV. It is seen that the major absorption starts from about 2.5 eV corresponding to the energy gap and the minor absorption begins at 1.18 eV. The 4d orbital of Fe atom is relatively far from the nucleus which is easy to overlap with the orbital of O atoms. The evidence of a few overlapping populations between Fe and O atoms is shown in Table 3. It is found that there may be minor electron occupying the states. On the basis of crystal field theory, in the FeO_6 octahedral the d orbital of Fe splits to threefold degeneracy t_{2g} and e_g bands. The PDOS of Fe displays two different states at the energy 2.6 eV (t_{2g} band) and 3.8 eV (e_g band), the energy difference is close to the minor absorption edge (shown in Fig. 6). It is indicated that the minor absorption happens when the electron is excited from t_{2g} bands to e_g bands.

The calculated real part $\varepsilon_1(\omega)$ and imaginary part $\varepsilon_2(\omega)$ of the dielectric function of BFO are shown in Fig. 7(a). It is seen that the imaginary part $\varepsilon_2(\omega)$ shows three peaks in the picture. The left peak is on account of the transition from O-p electron to unoccupied Fe-d states, the middle one is due to the transition from O-p electron to Bi-p high-energy conduction bands, and the right one is owing to the transition of inner electron excitation from O-p to Bi-p or Fe-d conduction bands [37,38]. The static dielectric constant $\varepsilon(0)$ is about 18 in this work. The loss function is shown in Fig. 7 (c). The peak of $L(\omega)$ is corresponding to the trailing edge in the reflection spectra. For instance, the prominent peak of $L(\omega)$ is situated at the energy about 30 eV corresponding the abrupt reduction of the reflectivity (shown in Fig. 7(b)). And it is also corresponding to the edge where $\varepsilon_2 < 1$ and ε_1 reaches the zero point. The main peak in $L(\omega)$ spectra represents the characteristic associated with the plasma response and corresponding frequency is the so-called plasma frequency ω_p.

The refractive index and the extinction coefficient are shown in Fig. 8. It is found that the static refractive index $n(0)$ is 4.2, the maximum of that is about 5.8 at 4 eV and the minimum of that is about 0.3 at 20 eV. As we know, the refractive index and extinction coefficient are in direct proportion to the real part and the imaginary part of the dielectric constant, respectively. Comparing Fig. 7(a) with Fig. 8, it can be found that two dash dot lines have the same trend, which indicates that the origin of the structures in the imaginary part of the dielectric function also explains the structures in the refractive index.

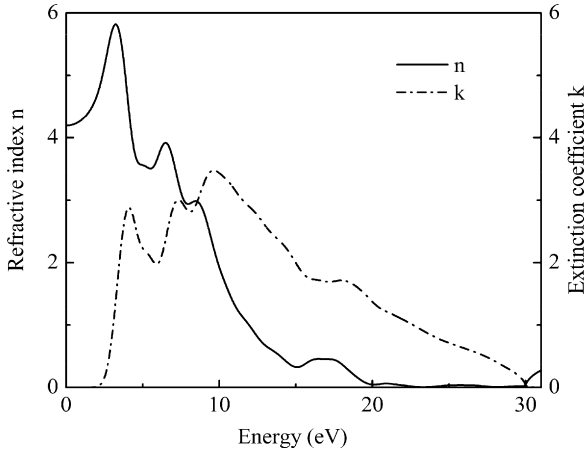

Fig. 8. Calculated optical refractive index n and extinction coefficient k of $BiFeO_3$.

4. Conclusions

In summary, the structural, electronic properties and optical properties of BFO were studied by employing the first-principles within generalized gradient approximations. The calculated equilibrium lattice constant was a little smaller than the experimental mean value. The electronic structure calculations showed that BFO had a 2.5 eV band gap. Analysis of the density of states revealed that the valence band was consisted with Fe-d and O-p states, and the conduction band was composed of Fe-d and Bi-p states. The covalence contributions between Fe and O atoms were more than between Bi–O atoms. The dielectric function, refractive index, reflectivity and electron energy loss were calculated for radiation up to 31 eV. It was indicated that the major absorption was believed to the transition from valence band to conduction bands and the reasons of the minor absorption were attributed to the electrons of the t_{2g} bands excited to the e_g bands.

Acknowledgements

This calculation was performed in the High Performance Computing Center of Northwestern Polytechnical University. This work has been supported by the National Nature Science Foundation (50672075), the NCET and 111 Program (B08040) of MOE, Xi'an Science and Technology Foundation (CXY08006, XA-AM-200905), the Fundamental Research Foundation (NPU-FFR-200703) of NPU, and the SKLSP Research Fund (40-QZ-2009) of China.

References

[1] J.H. Xu, H. Ke, D.C. Jia, W. Wang, Y. Zhou, J. Alloys Compd. 472 (2009) 473.
[2] K.F. Wang, J.M. Liu, Z.F. Ren, Adv. Phys. 58 (2009) 321.
[3] N. Kumar, N. Panwar, B. Gahtori, N. Singh, H. Kishan, V.P.S. Awana, J. Alloys Compd. 501 (2010) L29.
[4] W. Eerenstein, N.D. Mathur, J.F. Scott, Nature 442 (2006) 759.
[5] P. Ravindran, R. Vidya, A. Kjekshus, H. Fjellvåg, O. Eriksson, Phys. Rev. B 74 (2006) 224412.
[6] J.F. Scott, Nat. Mater. 6 (2007) 256.
[7] M. Bibes, A. Barthelemy, Nat. Mater. 7 (2008) 425.
[8] C.Y. Yang, J.S. Jiang, F.Z. Qian, D.M. Jiang, C.M. Wang, W.G. Zhang, J. Alloys Compd. 507 (2010) 29.
[9] G. Catalan, J.F. Scott, Adv. Mater. 21 (2009) 2463.
[10] S.L. Shang, G. Sheng, Y. Wang, L.Q. Chen, Z.K. Liu, Phys. Rev. B 80 (2009) 052102.
[11] J. Wang, J.B. Neaton, H. Zheng, V. Nagarajan, S.B. Ogale, B. Liu, D. Viehland, V. Vaithyanathan, D.G. Schlom, U.V. Waghmare, N.A. Spaldin, K.M. Rabe, M. Wutting, R. Ramesh, Science 299 (2003) 1719.
[12] T. Zhao, A. Scholl, F. Zavaliche, K. Lee, M. Barry, A. Doran, M.P. Cruz, Y.H. Chu, C. Ederer, N.A. Spaldin, R.R. Das, D.M. Kim, S.H. Baek, C.B. Eom, R. Ramesh, Nat. Mater. 5 (2006) 823.
[13] Y.H. Chu, L.W. Martin, M.B. Holcomb, M. Gajek, S.J. Han, Q. He, N. Balke, C.H. Yang, D. Lee, W. Hu, Q. Zhan, P.L. Yang, A. Fraile-Rodrguez, A. Scholl, S.X. Wang, R. Ramesh, Nat. Mater. 7 (2008) 478.
[14] Y. Du, Z.X. Cheng, M. Shahbazi, E.W. Collings, S.X. Dou, X.L. Wang, J. Alloys Compd. 490 (2010) 637.
[15] P. Uniyal, K.L. Yadav, J. Alloys Compd. 492 (2010) 406.
[16] A.Z. Simões, F.G. Garcia, C.S. Riccardi, J. Alloys Compd. 493 (2010) 158.
[17] J. Liu, M.Y. Li, L. Pei, J. Wang, B.F. Yu, X. Wang, X.Z. Zhao, J. Alloys Compd. 493 (2010) 544.
[18] S. Kazhugasalamoorthy, P. Jegatheesan, R. Mohandoss, N.V. Giridharan, B. Karthikeyan, R.J. Joseyphus, S. Dhanuskodi, J. Alloys Compd. 493 (2010) 569.
[19] X.Q. Zhang, Y. Sui, X.J. Wang, Y. Wang, Z. Wang, J. Alloys Compd. 507 (2010) 157.
[20] X.S. Xu, T.V. Brinzari, S. Lee, Y.H. Chu, L.W. Martin, A. Kumar, S. McGill, R.C. Rai, R. Ramesh, V. Gopalan, S.W. Cheong, J.L. Musfeldt, Phys. Rev. B 79 (2009) 134425.
[21] D.K. Mishra, X.D. Qi, J. Alloys Compd. 504 (2010) 27.
[22] P. Baettig, C. Ederer, N.A. Spaldin, Phys. Rev. B 72 (2005) 214105.
[23] L. Zhu, K.L. Yao, Z.L. Liu, D.H. Zhang, Phys. Lett. A 373 (2009) 2374.
[24] Y.L. Wang, Z.H. Wu, Z.C. Deng, L.Z. Chu, B.T. Liu, W.H. Liang, G.S. Fu, Ferroelectrics 386 (2009) 133.
[25] Z.Y. Wang, K.H. Su, H.Q. Fan, Z.Y. Wen, Polymer 48 (2007) 7145.
[26] J.P. Perdew, J.A. Chevary, S.H. Vosko, K.A. Jackson, M.R. Pederson, D.J. Singh, C. Fiolhais, Phys. Rev. B 46 (1992) 6671.
[27] J.P. Perdew, K. Burke, M. Ernzerhof, Phys. Rev. Lett. 77 (1996) 3865.
[28] E.A. Moore, Phys. Rev. B 76 (2007) 195107.
[29] D. Vanderbilt, Phys. Rev. B 41 (1990) 7892.
[30] I. Sosnowska, W. Schafer, W. kockelmann, K.H. Andersen, I.O. Troyanchuk, Appl. Phys. A 74 (2002) S1040.
[31] A. Reyes, C. de la Vega, M.E. Fuentes, L. Fuentes, J. Eur. Ceram. Soc. 27 (2007) 3709.
[32] D. Kothari, V.R. Reddy, V.G. Sathe, A. Gupta, A. Banerjee, A.M. Awasthi, J. Magn. Magn. Mater. 320 (2008) 548.
[33] D. Ricinschi, K.Y. Yun, M. Okuyama, J. Phys.: Condens. Matter 18 (2006) L97–L105.
[34] H.M. Tutuncu, G.P. Srivastava, J. Appl. Phys. 103 (2008) 083712.
[35] H. Wang, Y. Zheng, M.Q. Cai, H.T. Huang, H.L.W. Chan, Solid State Commun. 149 (2009) 641.
[36] S.J. Clark, J. Robertson, Appl. Phys. Lett. 90 (2007) 132903.
[37] A. Bouhemadou, R. Khenata, F. Djabi, Solid State Sci. 11 (2009) 556.
[38] H. Wang, H.T. Huang, B. Wang, Solid State Commun. 149 (2009) 1849.